

# Proper motion of H<sub>2</sub>O masers in IRAS 20050+2720 MMS1: an AU scale jet associated with an intermediate-mass class 0 source

R. S. Furuya<sup>1</sup>, Y. Kitamura<sup>2</sup>, A. Wootten<sup>3</sup>, M. J. Claussen<sup>4</sup>, and R. Kawabe<sup>5</sup>

<sup>1</sup> Division of Physics, Mathematics, and Astronomy, California Institute of Technology, MS 105-24, 1201 East California Boulevard, Pasadena, CA 91125, USA  
e-mail: rsf@astro.caltech.edu

<sup>2</sup> Institute of Space and Astronautical Science, Japan Aerospace Exploration Agency, Yoshinodai 3-1-1, Sagami-hara, Kanagawa 229-8510, Japan  
e-mail: kitamura@pub.isas.jaxa.jp

<sup>3</sup> National Radio Astronomy Observatory, 520 Edgemont Road, Charlottesville, VA 22903, USA  
e-mail: awootten@nrao.edu

<sup>4</sup> National Radio Astronomy Observatory, 1003 Lopezville Road, Socorro, NM 87801, USA  
e-mail: mcclaussen@nrao.edu

<sup>5</sup> National Astronomical Observatory, Osawa 2-21-1, Mitaka, Tokyo 181-8588, Japan  
e-mail: kawabe@nro.nao.ac.jp

Received 13 August 2003 / Accepted 26 March 2005

**Abstract.** We conducted a 4 epoch, 3 month, VLBA proper motion study of H<sub>2</sub>O masers toward an intermediate-mass class 0 source IRAS 20050+2720 MMS1 ( $d = 700$  pc). The region of IRAS 20050+2720 contains at least 3 bright young stellar objects at millimeter to submillimeter wavelengths and shows three pairs of CO outflow lobes: the brightest source MMS1, which shows an extremely high velocity (EHV) wing emission, is believed to drive the outflow(s). From milli-arcsecond (mas) resolution VLBA images, we found two groups of H<sub>2</sub>O maser spots at the center of the submillimeter core of MMS1. One group consists of more than  $\sim 50$  intense maser spots; the other group consisting of several weaker maser spots is located at 18 AU south-west of the intense group. Distribution of the maser spots in the intense group shows an arc-shaped structure which includes the maser spots that showed a clear velocity gradient. The spatial and velocity structures of the maser spots in the arc-shape did not significantly change through the 4 epochs. Furthermore, we found a relative proper motion between the two groups. Their projected separation increased by  $1.13 \pm 0.11$  mas over the 4 epochs along a line connecting them (corresponding to a transverse velocity of  $14.4 \text{ km s}^{-1}$ ). The spatial and velocity structures of the intense group and the relative proper motions strongly suggest that the maser emission is associated with a protostellar jet. Comparing the observed LSR velocities with calculated radial velocities from a simple biconical jet model, we conclude that the most of the maser emission is likely to be associated with an accelerating biconical jet that has large opening angle of about  $70^\circ$ . The large opening angle of the jet traced by the masers would support the hypothesis that poor jet collimation is an inherent property of luminous (proto)stars.

**Key words.** stars: formation – radio lines: ISM – ISM: jets and outflows – ISM: individual objects: IRAS 20050+2720 MMS1

## 1. Introduction

Water maser surveys using single-dish radio telescopes toward intermediate- and low-mass young stellar objects (YSOs) have been extensively performed since the early 1990s (e.g., Claussen et al. 1996). From a multi-epoch survey toward low-mass YSOs (bolometric luminosity,  $L_{\text{bol}} < 100 L_\odot$ ), Furuya et al. (2001, 2003) found that class 0 objects are favored sites for the masers: the detection rates are derived to be  $\sim 40\%$  for class 0, while only  $\sim 4\%$  for class I. It is known that the isotropic maser luminosity,  $L_{\text{H}_2\text{O}}$ , correlates well with the bolometric luminosity of the source (Wilking et al. 1994; Furuya et al. 2001). However, it is interesting to note that the presence of the maser emission is strictly related to that of

high-velocity outflowing gas in the case of high-mass YSOs (Felli et al. 1992). Furuya et al. (2001) showed that the H<sub>2</sub>O maser luminosity in low-mass stars is more closely related to the luminosity of 100 AU scale radio jets rather than the mechanical luminosity of larger scale CO outflows. In fact, VLA observations have revealed that the masers tend to be distributed within several hundred AU of the central stars (e.g., Wootten 1989). Although some H<sub>2</sub>O masers are reported to be associated with protostellar disks (e.g., Fiebig et al. 1996; Torrelles et al. 1998; Seth et al. 2002), high resolution VLBI observations have demonstrated the presence of knots and shock structures which are reminiscent of those of ionized jets in the larger scale Harbig Haro objects, suggesting that in most cases the masers originate in shocks produced by jets from

protostars (e.g., Claussen et al. 1998; Furuya et al. 2000). There are a few published VLBI water maser studies of the jets and outflows from intermediate-mass young stellar objects (Patel et al. 2000; Seth et al. 2002). In order to extend our knowledge of H<sub>2</sub>O masers in intermediate-mass YSOs, we have conducted multi-epoch VLBA observations of H<sub>2</sub>O masers towards the intermediate-mass YSO IRAS 20050+2720 ( $d = 700$  pc).

## 2. IRAS 20050+2720

IRAS 20050+2720 is surrounded by a large cluster of low-mass stars (Chen et al. 1997; Wilking et al. 1989) and has a luminosity in the IRAS bands of  $388 L_{\odot}$  (Molinari et al. 1996). The IRAS source has been categorized as a luminous class 0 protostar in the early compilation (Bachiller 1996). Recent SCUBA imaging (Chini et al. 2001) revealed the presence of a bright central object (IRAS 20050+2720 MMS1) and two associated objects located  $\sim 2'$  south-east. The brightest source MMS1 is identified as the IRAS source. Although IRAS 20050+2720 was not categorized as class 0 in the updated compilation (André et al. 2000), Chini et al. (2001) reported that the source MMS1 is very likely to be at the class 0 stage. This is because MMS1 shows a ratio of FIR luminosity ( $L_{\text{FIR}}$ ) and submillimeter luminosity ( $L_{\text{submm}}$ ) for  $\lambda \geq 350 \mu\text{m}$  of  $\sim 164$  which satisfies one of the definitions of class 0 (André et al. 1993;  $L_{\text{bol}}/L_{\text{submm}} \leq 200$ ).

Bachiller et al. (1995; hereafter BFT95) found three pairs of outflow lobes emanating from the vicinity of the source MMS1 from the IRAM 30-m telescope CO  $J = 2-1$  observations. One of the lobe pairs is a highly collimated jet with extremely high velocity (EHV) emission whose terminal velocity exceeds  $\sim 60 \text{ km s}^{-1}$  with respect to the ambient cloud velocity. The presence of the EHV outflow suggests that the driving source of the EHV outflow is in its most powerful outflow phase. BFT95 suggested that two or three independent outflows emanate from different YSOs embedded in the cloud core, although the driving sources have not been identified.

H<sub>2</sub>O maser emission in the IRAS 20050+2720 region was first detected by Palla et al. (1991), and was subsequently observed by the Arcetri group (Brand et al. 1994; Palumbo et al. 1994): all of the detected emission was seen around the cloud velocity ( $V_{\text{LSR}} = 6 \text{ km s}^{-1}$ ). Using the Nobeyama 45-m telescope, Furuya et al. (2003) detected EHV maser emission at  $V_{\text{LSR}} = -91 \text{ km s}^{-1}$ . The EHV emission was blueshifted with respect to the cloud velocity, while no high velocity emission was detected on the redshifted side. This source also showed weak, blueshifted, intermediate high velocity (IHV) components at  $V_{\text{LSR}} = -24$  and  $-36 \text{ km s}^{-1}$  in 1998 February. In 1999, we carried out VLA observations and found that all of the maser emission was located within  $\sim 5''$  ( $\sim 350 \text{ AU}$ ) from the source MMS1. Our VLA observations revealed that the EHV emission is located exactly at the JCMT position for source MMS1, while the low-velocity components around the cloud velocity are located to  $4.50''$  west and  $0.60''$  north of the EHV emission (Furuya et al. 2003). Suspecting multiplicity of CO outflows and the fact that the SCUBA beam ( $8.3''$  at  $450 \mu\text{m}$ ; Chini et al. 2001) is larger than the separation of the two maser components, we made high resolution continuum images of the

region with the OVRO mm-array. In order to investigate the detailed structure of the masers, we carried out extremely high angular resolution VLBA observations.

## 3. Observations

### 3.1. 3 mm continuum emission observations with OVRO mm-array

Aperture synthesis observations of continuum emission at 3 mm were carried out using the six-element Owens Valley Radio Observatory (OVRO) Millimeter Array from 2002 December to 2003 February with the H and E array configurations. The phase tracking center was  $\alpha(\text{J2000}) = 20^{\text{h}}07^{\text{m}}5^{\text{s}}.87$ ,  $\delta(\text{J2000}) = 27^{\circ}28'59''.80$ . The field of view (FOV) was  $65''$ . All of the element antennas are equipped with SIS receivers having system noise temperatures in double-sideband of 200 K toward the zenith at 93 GHz. We tuned the 3 mm SIS receiver at the frequencies of N<sub>2</sub>H<sup>+</sup> (1–0) line (93.173 GHz) for the upper sideband and H<sup>13</sup>CO<sup>+</sup> (1–0) line (86.754 GHz) for the lower sideband. A detailed presentation of the results of the molecular line emission will be published elsewhere (Furuya et al., in preparation). The Continuum Correlator was configured for both the sidebands, with a total bandwidth of 3 GHz. We used 3C454.3 and 3C84 as a passband calibrator and J2025+337 as a phase and gain calibrator. Flux density of J2025+337 was measured by comparison to that of Uranus: it was stable in the range from 1.2 to 1.5 Jy during the observation period. The overall flux uncertainty is about 20%. The data calibration was done using originally developed software at OVRO, and the image construction was performed using the AIPS package of the NRAO. After merging the data in both the sidebands, we constructed continuum emission images with two beam weightings. Synthesized beam sizes were  $4''.04 \times 3''.18$  with natural weighting and  $2''.60 \times 1''.85$  with uniform weighting. The  $1\sigma$  rms noise levels for the continuum emission maps were  $0.78 \text{ mJy beam}^{-1}$  for the former and  $1.5 \text{ mJy beam}^{-1}$  for the latter.

### 3.2. H<sub>2</sub>O maser observations with VLBA

VLBI observations of the H<sub>2</sub>O maser emission in IRAS 20050+2720 MMS1 were carried out using all 10 antennae of the Very Long Baseline Array (VLBA) of the NRAO<sup>1</sup> on 1999 April 1, May 5, June 5, and July 4 (hereafter epochs I, II, III and IV, respectively). For epoch II, however, we could not use the antenna at North Liberty. All of the data were obtained for 8-h integration each epoch. We used a frequency setup of the 8 MHz IF bandwidth mode with 512 channels, which provides a velocity resolution of  $0.2 \text{ km s}^{-1}$  at 22.235077 GHz. This frequency setup covers the range of  $V_{\text{LSR}} = -96.1$  to  $+10.5 \text{ km s}^{-1}$ : this velocity coverage is sufficient to detect all of the maser emission previously detected.

<sup>1</sup> The National Radio Astronomy Observatory (NRAO) is operated by Associated Universities, Inc., under cooperative agreement with the National Science Foundation.

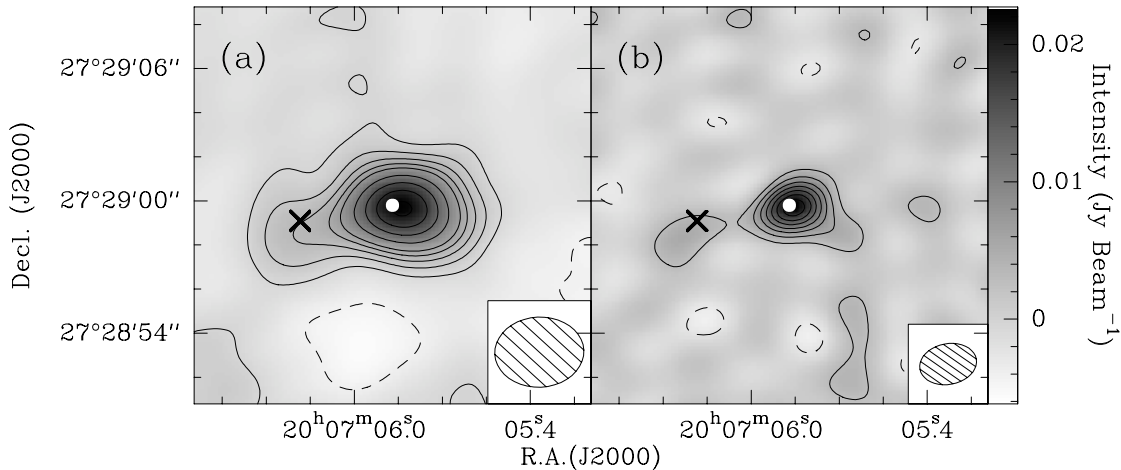


**Fig. 1.** Continuum emission maps taken with the OVRO millimeter array toward IRAS 20050+2720 MMS1 with **a)** natural weighting (*left*) and **b)** uniform weighting (*right*). The solid contours start at  $+2\sigma$  level with  $+2\sigma$  interval and the dashed contours are  $-2\sigma$  intervals started at  $-2\sigma$  level. The image noise levels are 0.78 and 1.5 mJy beam<sup>-1</sup> for the panels **a)** and **b)**, respectively. The white dot and the eastern cross indicate the positions of the low-velocity and EHV H<sub>2</sub>O maser emission (see Sect. 4.2.2). The sizes of the synthesized beams are presented in the bottom right corners.

The data were correlated at the NRAO Array Operation Center (Socorro, New Mexico). We adopted a correlator averaging time of 2.16 s to obtain  $\sim 0.8''$  radius FOV for the baseline of  $\sim 4000$  km. Data calibration and image construction were performed using the AIPS package developed by the NRAO. We used two bright quasars 3C 345 and 3C 454.3 to determine delay and fringe rates as well as to calibrate bandpass response. In the next section, we present the image construction, identification of the maser emission and further analysis together with the results.

## 4. Results and analyses

### 4.1. Relation between millimeter continuum emission and masers

Figure 1 presents the OVRO continuum emission maps together with the positions of the H<sub>2</sub>O masers. There is a distinct continuum emission peak toward the low-velocity and EHV maser emission. To plot the absolute position of the low-velocity masers, we adopted the results from the VLA measurements by Furuya et al. (2003) and used the position offset of the EHV emission obtained in Sect. 4.2.2. Clearly the millimeter continuum emission is associated with the low-velocity maser emission. The peak of the continuum emission is slightly shifted with respect to the maser emission. We believe that this positional shift is real considering the baseline accuracies of VLA and OVRO array and angular separations between the calibrators and the source. It is noteworthy that the continuum emission in the natural weighting map (Fig. 1a) is elongated to the east, namely, toward the EHV emission. In the uniform weighting map (Fig. 1b), one may notice that there is a weak emission peak close to the EHV maser emission: this fact might suggest that there are at least two YSOs in this region.

We estimate molecular hydrogen mass ( $M_{\text{H}_2}$ ) of the core from the total flux density ( $F_\nu$ ) of the continuum emission assuming that the emission is thermal radiation from dust grains.

We used a relation  $M_{\text{H}_2} = F_\nu D^2 / (\kappa_\nu B_\nu(T_d))$  where  $\kappa_\nu$  is the mass opacity coefficient of the dust,  $T_d$  is the dust temperature and  $B_\nu(T_d)$  is the Planck function. The value of  $\kappa_\nu$  at 3 mm is calculated with the usual form of  $\kappa_\nu \propto \kappa_0 \nu^\beta$ . In order to keep consistency with the previous JCMT measurements by Chini et al. (2001), we used the same  $\kappa_0$  of 0.003 cm<sup>2</sup> g<sup>-1</sup> at 231 GHz,  $\beta$  of 1.4, and  $T_d$  of 34 K. We obtained  $M_{\text{H}_2}$  of 0.007  $M_\odot$  for  $F_\nu = 25.6$  mJy by integrating the emission inside the  $3\sigma$  contour. Note that the derived mass is a lower limit because interferometric observations do not receive the whole flux from a source due to the lack of short spatial frequency data. In fact, the resultant projected baseline length of our OVRO observations ranged from 6.2 to 75 k $\lambda$ , which will miss 50% of the flux from structures extending more than 16'' (0.05 pc at  $d = 700$  pc) (see Wilner & Welch 1994).

### 4.2. Maser emission search in the VLBA data: Low and extremely high velocity emission

In the following, we present results and analyses from the VLBA observations of the H<sub>2</sub>O masers.

First, we carried out fringe-frequency analysis (e.g., Walker 1981; Walker et al. 1982) to cover a large FOV of  $\sim 3''$  which is 3 orders of magnitude larger than the VLBA fringe-spacings. The purpose of the fringe-frequency analysis was to search for maser spots which were not excited during the VLA observations in 1999 February (Furuya et al. 2003). As expected from the VLA observations, we confirmed that the distribution of the low-velocity masers is sufficiently compact to perform standard Fourier synthesis. The EHV emission was too weak to be detected with the fringe-frequency analysis.

Subsequently, we performed self-calibration using a strong ( $\sim 45$  Jy measured by Furuya et al. 2003) and point-like maser spot identified at  $V_{\text{LSR}} = +1.6$  km s<sup>-1</sup> as a model. In the self-calibration procedure, we solved the time variation of the complex gain for phase weighted by amplitude.

**Table 1.** Summary of VLBA H<sub>2</sub>O maser observations.

Epoch <sup>a</sup>	MAIN Field: Low-Velocity Emission				Sub-Field <sup>b</sup> : EHV Emission			
	Number of antennas	$\theta_{\text{maj}} \times \theta_{\text{min}}$ (mas $\times$ mas)	PA (deg)	Sensitivity <sup>c</sup> (mJy beam <sup>-1</sup> )	Number of antennas	$\theta_{\text{maj}} \times \theta_{\text{min}}$ (mas $\times$ mas)	PA (deg)	Sensitivity <sup>c</sup> (mJy beam <sup>-1</sup> )
I	10 <sup>d</sup>	0.78 $\times$ 0.40	-2	3.4	5 <sup>f</sup>	2.8 $\times$ 1.4	+29	6.2
II	9 <sup>e</sup>	1.1 $\times$ 0.51	+26	3.7	5 <sup>f</sup>	2.8 $\times$ 1.5	+29	4.7
III	10 <sup>d</sup>	0.95 $\times$ 0.40	-14	2.8	5 <sup>f</sup>	2.9 $\times$ 1.6	+24	4.8
IV	10 <sup>d</sup>	1.1 $\times$ 0.39	-14	3.5	5 <sup>f</sup>	2.9 $\times$ 1.6	+27	6.9

<sup>a</sup> The 4 epochs are 1999 April 1, May 5, June 5 and July 4. <sup>b</sup> The following data are common for the Sub-Fields 1 and 2 (see Sect. 4.2.2). <sup>c</sup> An rms image noise level with a velocity resolution of 0.2 km s<sup>-1</sup>. <sup>d</sup> All 10 VLBA stations. <sup>e</sup> Except the North Liberty station. <sup>f</sup> Fort Davis, Los Alamos, Pie Town, Kitt Peak and Owens Valley.

#### 4.2.1. Main field: Low-velocity emission

Applying the solutions from the self-calibration procedure, we carried out image construction toward the low-velocity emission (hereafter we refer to it as the MAIN Field): the image area has  $\sim 0.23''$  size divided into 9 fields each of which is of 77 milli-arcsecond (mas) size and  $512 \times 512$  pixels with a cell size of 0.15 mas. We believe that the area size of  $\sim 0.23''$  was sufficient to search for maser emission considering the absolute position accuracy of the VLA observations (Sect. 2). Subsequent to this coarse search, we constructed a final image of 41 mas size for the area where the low-velocity emission was detected, with a smaller cell size of 0.08 mas. The image noise level per velocity channel was typically 3 mJy beam<sup>-1</sup> and the synthesized beam size was typically  $1.0 \times 0.5$  mas (Table 1).

In Fig. 2, we show a total integrated intensity map of the MAIN Field, namely low-velocity H<sub>2</sub>O masers, obtained in the Epoch III, in which we attained the highest sensitivity among the 4 epochs. The inserted panel presents the spectrum of the maser emission detected in the region. The overall distribution of the masers was similar for all 4 epochs: we see bright maser emission peaks at the field center (hereafter MAIN group) and an isolated emission peak at  $\sim 25$  mas (corresponding to  $\sim 18$  AU) south-west of the MAIN group. Hereafter we call the latter emission the “SW feature” instead of “SW group” because the emission showed a point-like structure. The definition of “feature” will be given in Sect. 4.3.

#### 4.2.2. Extremely high velocity emission

In addition, we searched for the EHV emission on the basis of the snapshot VLA D-array observations in 1999 February (Furuya et al. 2003) and 2003 January (Claussen, private communication): the former observations (hereafter Sub-Field 1) showed that the  $V_{\text{LSR}} = -93$  km s<sup>-1</sup> emission is shifted by  $+2.33''$  in RA and  $-0.60''$  in Dec with respect to the low-velocity emission and the latter observations (hereafter Sub-Field 2) showed that the  $V_{\text{LSR}} = -72$  and  $-78$  km s<sup>-1</sup> emission is shifted by  $+4.4''$  in RA and  $-0.6''$  in Dec. Since these positions are outside the FOV correlated with the 1.6 km s<sup>-1</sup> emission, we used UV data only from south-western 5 antennas (Fort Davis, Los Alamos, Pie Town, Kitt Peak and Owens Valley) which provide a maximum spatial frequency of  $\sim 1.1 \times 10^8 \lambda$ . The synthesized beam sizes were typically

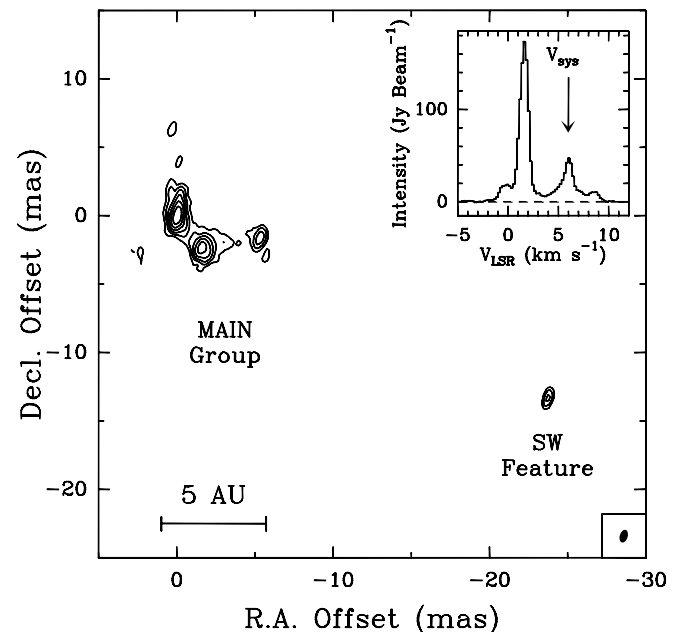


**Fig. 2.** Total integrated intensity map of the H<sub>2</sub>O masers in the MAIN Field of IRAS 20050+2720 MMS1 obtained at the 3rd epoch (1999 June 5) of the VLBA observations. Contour levels are 10, 20, 30, 50, 100, 200, 400, 800, 1600, 3200, 6400, 12 800 and 25 600 times the image noise level of 12.3 mJy beam<sup>-1</sup> km s<sup>-1</sup>. The inserted panel in the top right corner shows the H<sub>2</sub>O maser spectrum obtained by integrating the emission over the presented region. The vertical arrow shows the ambient cloud velocity ( $V_{\text{sys}}$ ) of  $V_{\text{LSR}} = 6.0$  km s<sup>-1</sup> estimated from CS  $J = 3-2$  line observations (BFT95). The size of the synthesized beam is presented in the bottom right corner.

$2.8 \times 1.5$  mas and the image noise levels per velocity channel were typically 5 mJy beam<sup>-1</sup> (Table 1). Applying the solution from the self-calibration procedure above, we constructed images toward both the Sub-Fields.

We detected the maser emission peaking of  $V_{\text{LSR}} = -93$  km s<sup>-1</sup> in Sub-Field 2 where the  $V_{\text{LSR}} = -72$  and  $-78$  km s<sup>-1</sup> emission was detected with the VLA in 2003 January. However, we did not see any maser emission around  $V_{\text{LSR}} = -72$  and  $-78$  km s<sup>-1</sup> toward the two Sub-Fields. The detected  $-93$  km s<sup>-1</sup> emission shows a point-like structure located at  $\sim 4184$  mas east and  $\sim 709$  mas south with respect to the  $V_{\text{LSR}} = 1.6$  km s<sup>-1</sup> emission peak with which we performed the self-calibration.

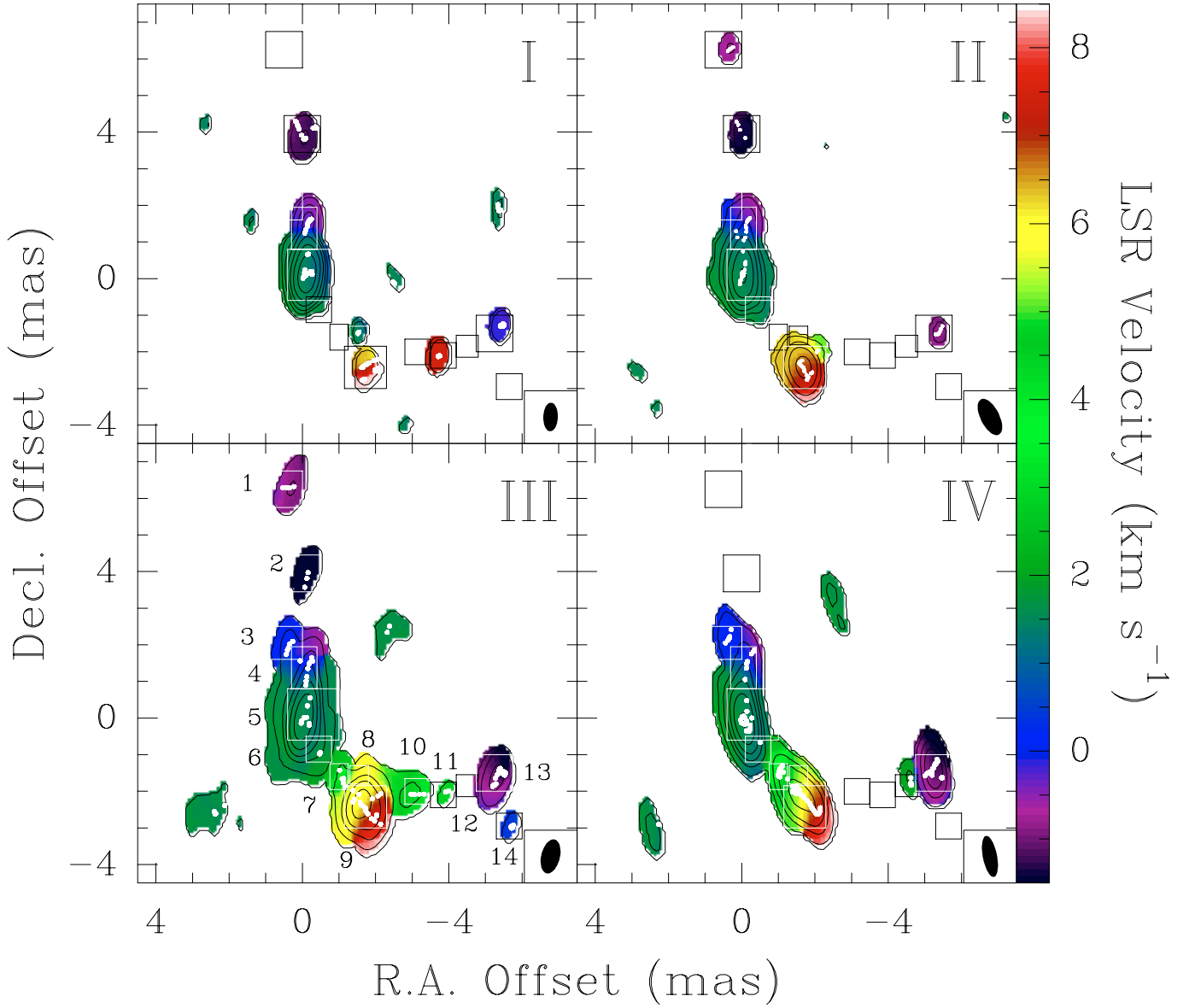


**Fig. 3.** Total integrated intensity maps (contours) overlaid with isovelocity maps (images) for the MAIN Field of the H<sub>2</sub>O masers in IRAS 20050+2720. The contour levels are the same as those in Fig. 2. The velocity range shown here is from  $V_{\text{LSR}} = -1.5$  to  $8.5 \text{ km s}^{-1}$ . The white dots present peak positions of the maser spots. Boxes with labels indicate identified maser features.

#### 4.3. Identification of maser spots and features

To identify maser “spots” from the image, we fitted a two-dimensional elliptical Gaussian profile to individual possible spots. We adopted a detection threshold of a signal-to-noise ratio ( $S/N$ ) larger than 10. In this way, we detected 30  $\sim$  70 maser spots at each epoch (Fig. 3). We estimated the relative positional error for each spot ( $\sigma_{\text{spot}}$ ) to be  $\leq 0.02$  mas: the relative positional error of a point-like source convolved with a Gaussian shaped beam is given by the relation of  $\sigma = 0.45 \theta_{\text{syn}}/[S/N]$  (Condon 1997) where  $\theta_{\text{syn}}$  is the  $FWHM$  of the synthesized beam ( $\theta_{\text{syn}} = [\theta_{\text{maj}} \times \theta_{\text{min}}]^{1/2}$ ).

Subsequent to the identification of the maser “spots”, we divided them into groups, i.e., spatially localized “features” with distinct peaks in line profiles: we grouped the spots in

adjacent velocity channels that are distributed within one synthesized beam width. Each feature is considered probably to represent a distinct clump of gas. In Fig. 3, only Features 4, 5, 9 and 13 showed emission over the 4 epochs among the 14 features identified in the MAIN-Field. Feature 2 persisted from Epoch I to III, but disappeared in Epoch IV. The other 9 features did not persist continuously more than 3 epochs. Therefore, we do not consider these 9 features in our further analysis of proper motion measurements. For each feature, we calculated an intensity-weighted mean position of the contributing maser spots: its uncertainty is given by  $\sigma_{\text{feature}} = [\sum_{\text{spot}} \sigma_{\text{spot}}^2]^{1/2}$ . As summarized in Table 2, the resultant positional errors were a few  $\times 0.01$  mas for the 6 features in the MAIN-Field and a few  $\times 0.1$  mas for the EHV feature in the Sub-Field.

**Table 2.** Relative positions of the identified H<sub>2</sub>O maser features.

Features	Epoch I			Epoch II			Epoch III			Epoch IV		
	$\Delta\alpha^a$	$\Delta\delta^b$	$\sigma^c$	$\Delta\alpha$	$\Delta\delta$	$\sigma$	$\Delta\alpha$	$\Delta\delta$	$\sigma$	$\Delta\alpha$	$\Delta\delta$	$\sigma$
	(mas)	(mas)	(mas)	(mas)	(mas)	(mas)	(mas)	(mas)	(mas)	(mas)	(mas)	(mas)
2	-0.046	3.928	0.011	0.049	4.094	0.014	-0.133	3.860	0.012	...	...	...
4	-0.160	1.500	0.031	-0.124	1.434	0.010	-0.154	1.308	0.012	-0.172	1.510	0.008
5	-0.133	0.135	0.008	-0.034	0.113	0.009	-0.053	-0.021	0.018	-0.071	-0.037	0.019
9	-1.794	-2.481	0.014	-1.679	-2.436	0.012	-1.659	-2.398	0.019	-1.684	-2.204	0.010
13	-5.439	-1.280	0.010	-5.392	-1.464	0.016	-5.349	-1.600	0.023	-5.235	-1.395	0.019
SW	-23.11	-12.89	0.052	-23.43	-13.10	0.04	-23.62	-13.50	0.03	-23.97	-13.60	0.05
EHV	4184.8	-709.9	0.29	4184.3	-709.9	0.35	4183.9	-709.7	0.18	4183.6	-709.4	0.17

<sup>a</sup> Right Ascension offset with respect to the 1.6 km s<sup>-1</sup> spot. <sup>b</sup> Declination offset. <sup>c</sup> Position error.

There is a velocity gradient of approximately 9 km s<sup>-1</sup> over 10 mas from Features 1 to 9.

#### 4.4. Spectra of the features and their time variation

For each maser feature identified, we obtained a spectrum by integrating the intensity over the corresponding region. Figure 4 represents spectra of the features listed in Table 2. Among the series of the 7 spectra, Features 2, 5 and EHV showed single-peaked spectra while Features 4, 9, 13 and SW displayed multi-peaked spectra. Using these spectra, we evaluated intensity-weighted mean velocities ( $V_{\text{mean}}$ ; Table 3). The former single-peaked features did not show any prominent trend of LSR-velocity change over the 4 epochs. On the other hand, the latter multiple-peaked features displayed small drifts. We discuss the velocity drifts when we assess proper motions of the features in the next subsection.

#### 4.5. Proper motions

Since VLBI observations generally do not provide absolute positions, we adopt the brightest spot at  $V_{\text{LSR}} = 1.6 \text{ km s}^{-1}$  in Feature 5 as a reference to examine the cross-epoch positional shifts of the maser features. The selection of the 1.6 km s<sup>-1</sup> spot is justified because this spot does not show any velocity drift over the 4 epochs. In addition, the spot is enough small to be used as a position reference as shown in the following. The correlated flux (i.e., fringe amplitude) of the spot drops by a factor of 2 at a projected baseline length of  $\sim 3.2 \times 10^8 \lambda$  which corresponds to a fringe spacing of  $\sim 0.06 \text{ mas}$ . This means that  $FWHM$  of the maser spot would be  $\sim 0.06 \text{ mas}$  assuming that the spot has a Gaussian shape brightness distribution. Note that the reference spot is not a complete point source compared with the relative position accuracy of the features (Table 2). Therefore, the size of the reference spot will be treated as a positional uncertainty in our analyses.

In Fig. 5, we present an overlay of the peak positions of the maser spots together with boxes indicating the identified features. The overall distribution of the maser spots does not change over the 4 epochs: it shows an arc-shaped structure. In Fig. 6, we present magnified overlays of the 7 features together with the intensity-weighted mean positions for the observing epochs (Table 2). As expected from Fig. 5, most of the maser

**Table 3.** Mean LSR-velocities<sup>a</sup> ( $V_{\text{mean}}$ ) for the identified maser features.

Feature	$V_{\text{mean}}$ (km s <sup>-1</sup> )			
	I	II	III	IV
2	-1.2	-1.1	-1.8	...
4	-0.39	-0.30	-0.23	-0.1
5	1.6	1.6	1.6	1.6
9	7.5	7.0	6.4	6.1
13	-0.30	-1.0	-1.6	-1.1
SW	3.5	2.9	2.9	1.8
EHV	-91.2	-91.3	-91.2	-91.3

<sup>a</sup> Errors are typically less than 0.03 km s<sup>-1</sup>.

features in the MAIN Group do not show any prominent positional shifts. On the other hand, Features SW and EHV displayed distinct positional shifts as can be seen in Fig. 6: the member spots of SW sequentially appeared from NE to SW over the 4 epochs and those of EHV appeared from SE to NW. These facts strongly suggest that the observed position shifts are caused by real motions of the spatially localized masing gas. In contrast, Features 2, 4 and 5 show neither well-defined position shifts of member spots nor systematic motions of their intensity-weighted mean positions.

In order to identify proper motions more quantitatively, we made plots of the intensity-weighted mean positions vs. time (Fig. 7). Table 4 summarizes the results of our analysis: we showed the derived position displacements for the 7 features. After the fifth column, we show results only for the maser features identified to have proper motions. We consider that the position shifts seen only in Features SW and EHV represent real motions of masing gas because these features displayed position shifts in  $|\mu|$  exceeding  $3\sigma$  levels of the uncertainties. In Table 4, we present position angles of the proper motions and transverse velocities ( $V_{\text{trans}}$ ) in the plane of the sky. In addition, we estimated 3D velocities ( $V_{3D}$ ) and the inclination angle ( $i$ ) to the plane of the sky.

On the other hand, we conclude that the mean position shifts of the Features 9 and 13 are not real gas motions, but apparent changes because their spot distributions seem *random*. Let us suppose maser appearance reflects the motions of shock fronts through a gas clump, as seems likely. Then the observations may have caught the clump harboring Feature 9 as one

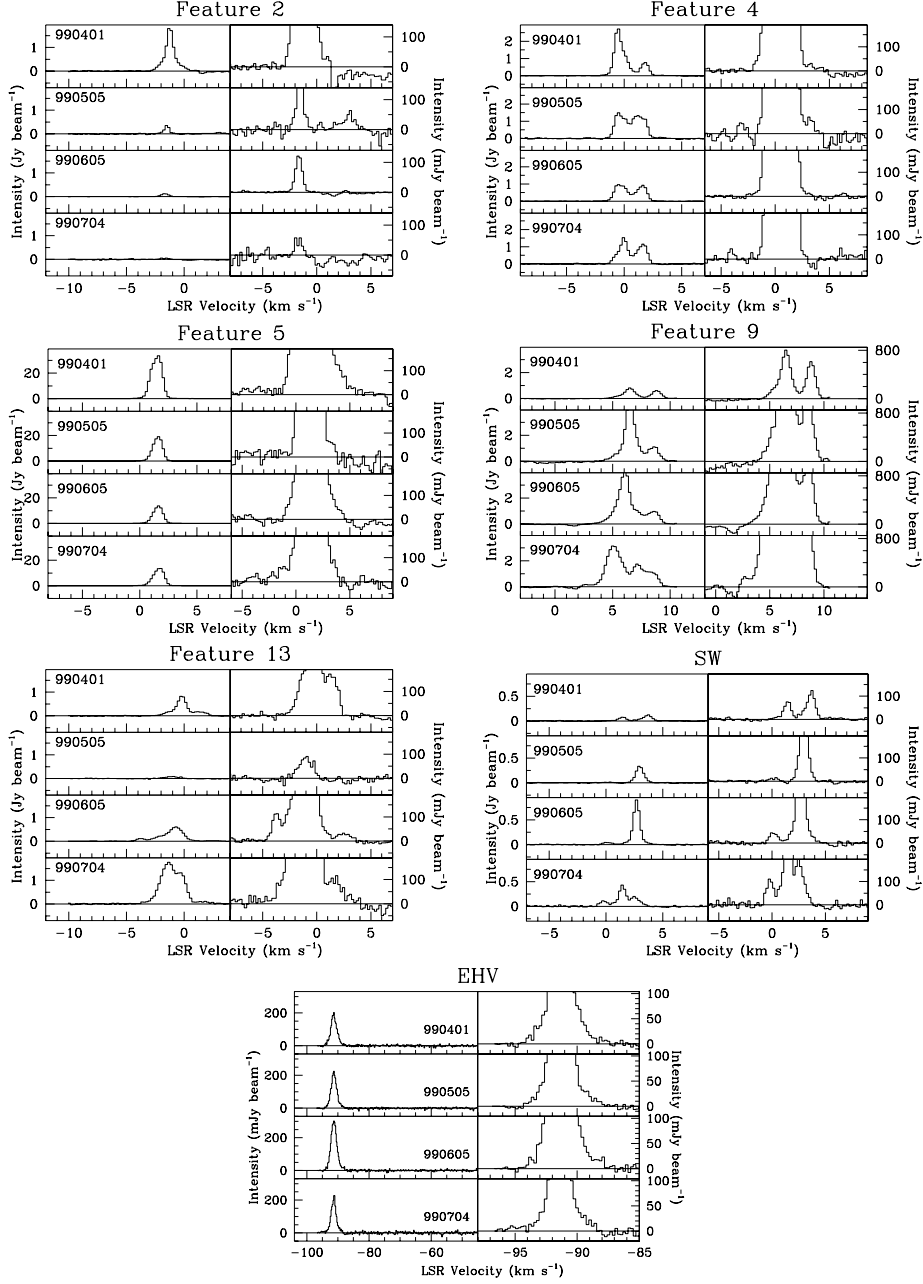


**Fig. 4.** H<sub>2</sub>O maser spectra toward Features 2, 4, 5, 9, 13, SW and EHV in IRAS 20050+2720 MMS1. The ambient cloud velocity is  $V_{\text{LSR}} = 6.0 \text{ km s}^{-1}$  (BFT95). In each feature, the spectra in the left-hand panels are magnified in the right-hand panels.

shock dies out in epoch I (e.g. SE-NW line of maser spots in Fig. 6) and as another becomes dominant in epochs II, III and IV (e.g. NE-SW line of maser spots in Fig. 6). In this interpretation, there appears to be little proper motion between epochs II and III, however there does appear to be some between epochs III and IV. Since the status of these aspects of Feature 9 remain unclear, we do not include them in our analysis of proper motions. A dataset with more closely spaced observations, extending over a similar time period, could possibly clarify the situation.

#### 4.6. Results of EHV maser emission

In Sect. 4.5, we showed that the observed position shift of the EHV maser emission is the proper motion of masering gas. The

proper motion of the EHV masers is directed almost towards the MAIN feature when we compare Figs. 1 with 6. Together with its line of sight velocity, we estimate that 3D motion of the masering gas has inclination angle of  $79.4^\circ \pm 0.4^\circ$  with respect to the plane of the sky (Table 4), suggesting that the gas motion is closely parallel to the line of sight. Applying the inclination to the apparent angular separation of  $\sim 4.2''$  between the MAIN and EHV (Table 4; corresponding to  $\sim 2900 \text{ AU}$  at  $d = 700 \text{ pc}$ ), their 3D separation is estimated to be approximately  $23''$  ( $\approx 16\,000 \text{ AU} \approx 0.078 \text{ pc}$ ). Even considering possible uncertainties, the real separation is very likely to be in the range between  $\sim 2900 \text{ AU}$  and  $\sim 16\,000 \text{ AU}$ .

We argue that the EHV masers represent a different protostar activity from the Main for the following reasons. First, the

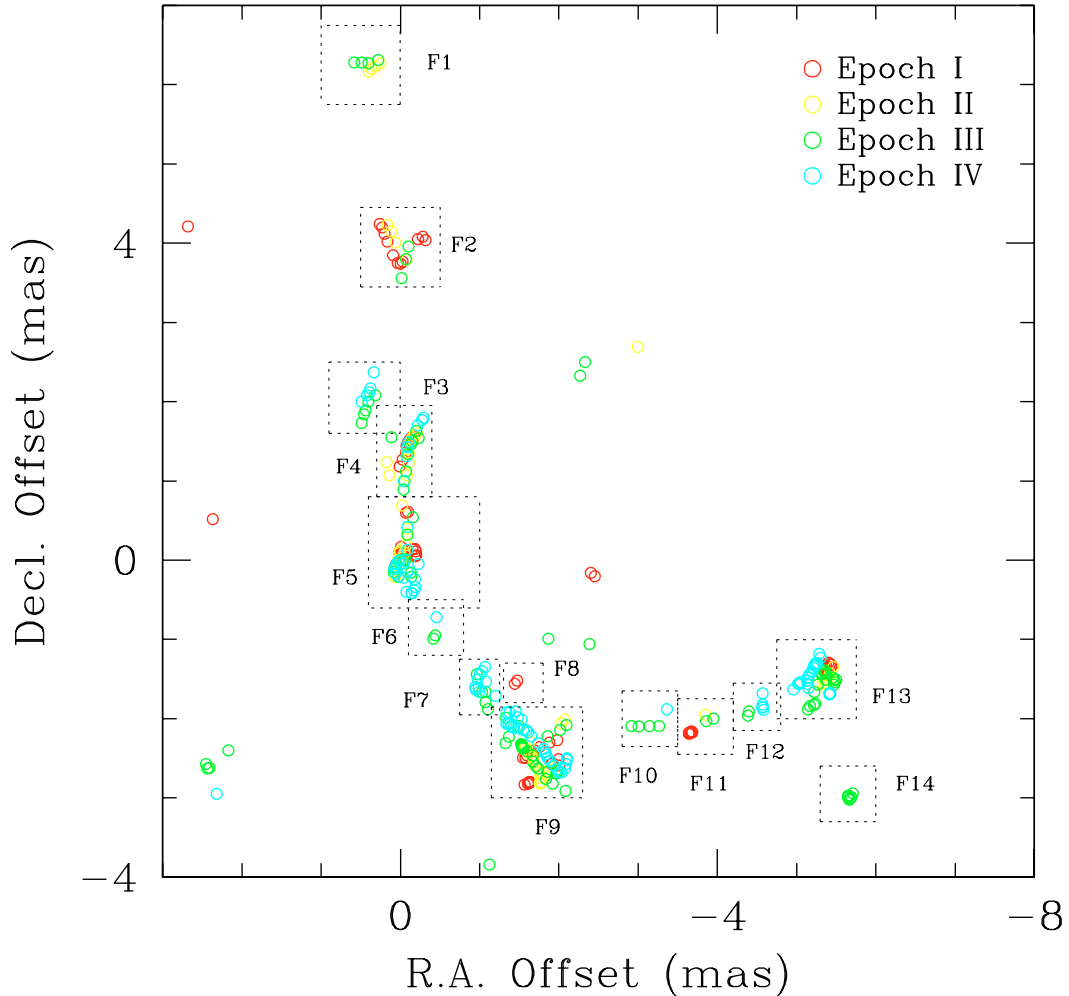


**Fig. 5.** Overlay of the peak positions of the low-velocity H<sub>2</sub>O maser spots in the MAIN-Field of IRAS 20050+2720 MMS1. The colors present the observing epochs and the dashed-boxes indicate the maser features identified in Sect. 4.3. The dashed-boxes are the same as the solid boxes in Fig. 3.

separation is too large to associate the EHV masers with the Main feature, which is likely to be excited by the intermediate-mass protostar (Sect. 2). In fact, Furuya et al. (2003) reported that all twenty H<sub>2</sub>O maser sources detected in their VLA survey toward low- and intermediate-mass YSOs were associated with the central protostars within  $\lesssim 50 \sim 200$  AU (see, e.g., Terebey et al. 1992). On the other hand, Hofner & Churchwell (1996) showed that the median separation between H<sub>2</sub>O masers and ultra compact HII regions is 0.1 pc for OB stars. Clearly, these facts support the above conclusion. Second, if masers originate of the larger scale EHV CO outflows from the MAIN, we could have observed expanding motion. However, our proper motion measurements clearly showed that their separation has decreased. On the basis of the large separation and the direction of proper motions, we thus rule out the hypothesis that EHV masers are associated with the jet emanating from the MAIN. We suggest that the EHV masers must be associated with another member source in the cluster (Chen et al. 1997; Wilking et al. 1989).

In order to search for the possible exciting source of the EHV maser emission, we analyzed 4.86 GHz radio continuum emission data from the VLA Archive Database. However, we

could not detect a compact radio continuum emission with a  $3\sigma$  upper limit of  $0.14 \text{ mJy beam}^{-1}$  ( $\theta_{\text{maj}} \times \theta_{\text{min}} \approx 5.97'' \times 5.15''$ ). On the basis of the lack of a bright compact continuum source and the presence of the EHV maser emission, we speculate that the driving source of the EHV emission could be an extremely young protostar.

## 5. Discussion

Evidence from AU-scale VLBI H<sub>2</sub>O maser observations suggests that the masers in star-forming regions are most likely to be excited in the interaction zone between a jet and ambient cloud material, or in interaction between a wide angle flow and the surface of a protostellar disk.

In this section, we discuss the origin of H<sub>2</sub>O masers associated with the millimeter continuum source MMS1 in terms of the jet scenario, supported by the following evidence. We do not further discuss the EHV maser emission which we have shown to be associated with other YSO activity (Sect. 4.6). We first note that the spatial and velocity structures of Features 2 to 12 in the MAIN group (Fig. 3) convincingly demonstrate that they are excited in outflowing gas associated with

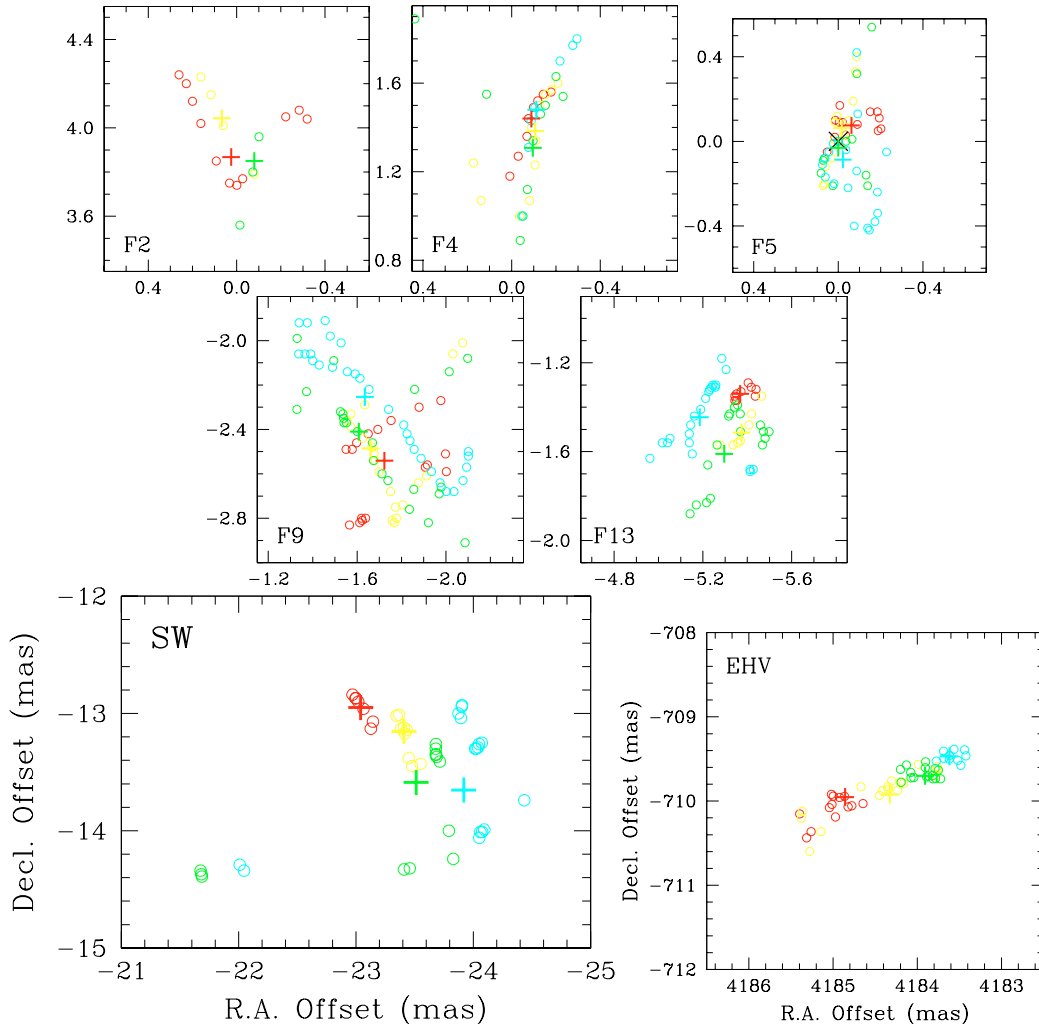


**Fig. 6.** Overlay of the peak positions of the maser spots in Features 2, 4, 5, 9, 13, SW and EHV where the maser emission was detected continuously more than 3 epochs. The colors indicate the observing epochs as in Fig. 5. Each color-coded plus mark indicates the intensity-weighted mean position of the features at each observing epoch. The black cross in Feature 5 indicates the adopted positional reference spot at  $V_{\text{LSR}} = 1.6 \text{ km s}^{-1}$ .

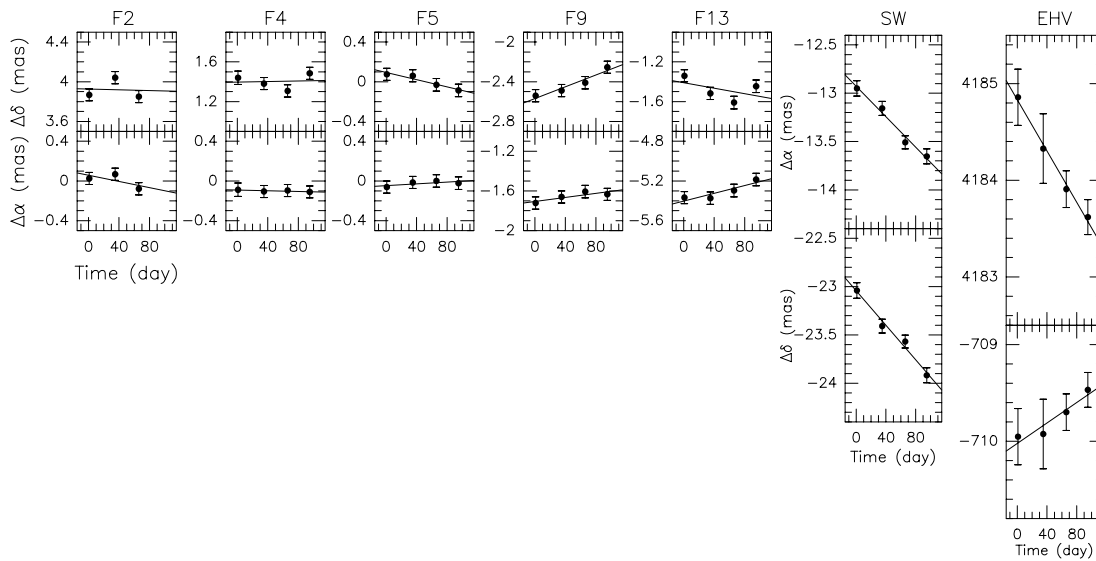


**Fig. 7.** Plots of intensity-weighted mean positions of the 7 features vs. time. Error bars include the positional uncertainties in Table 2 and the size of the reference spot at  $1.6 \text{ km s}^{-1}$  (Sect. 4.5). The straight lines are the best-fit to the data. The origin of the time axis is 1999 April 1.

**Table 4.** Position shifts and proper motions for the 7 maser features.

Feature	$\Delta\alpha^a$ (mas)	$\Delta\delta^b$ (mas)	$ \mu ^c$ (mas)	PA <sup>d</sup> (deg)	$V_{\text{trans}}^e$ (km s <sup>-1</sup> )	$V_{3\text{D}}^f$ (km s <sup>-1</sup> )	$i^g$ (deg)
2 <sup>h</sup>	$-0.018 \pm 0.31$	$-0.15 \pm 0.16$	$(0.15 \pm 0.35)$	...	...	...	...
4	$0.013 \pm 0.13$	$-0.017 \pm 0.011$	$(0.021 \pm 0.14)$	...	...	...	...
5	$-0.17 \pm 0.034$	$0.042 \pm 0.03$	$(0.18 \pm 0.076)$	...	...	...	...
9	$0.28 \pm 0.058$	$0.098 \pm 0.043$	$(0.30 \pm 0.094)$	...	...	...	...
13	$-0.13 \pm 0.017$	$0.19 \pm 0.062$	$(0.23 \pm 0.06)$	...	...	...	...
SW	$-0.75 \pm 0.078$	$-0.85 \pm 0.085$	$1.13 \pm 0.11$	-131.4	$14.4 \pm 1.4$	$14.4 \pm 1.4$	$4.7 \pm 3.5$
EHV	$-0.50 \pm 0.12$	$+1.26 \pm 0.085$	$1.36 \pm 0.16$	-68.2	$17.9 \pm 5.2$	$-91.3 \pm 29.5$	$79.4 \pm 0.2$

<sup>a</sup> and <sup>b</sup> total position shifts of the maser features over the observing period, namely per 95 days, along RA and Dec directions, respectively, derived from the least-square fitting in Fig. 7. <sup>c</sup>  $|\mu| = \sqrt{(\Delta\alpha)^2 + (\Delta\delta)^2}$ . For the maser features where we could not detect well-defined proper motions, apparent position shifts are given in the parenthesis. <sup>d</sup> Position Angle of the proper motion vector in the plane of the sky. <sup>e</sup> Transverse velocity on the plane of the sky converted from  $|\mu|$ . <sup>f</sup> 3-Dimensional velocity obtained from  $V_{3\text{D}} = \sqrt{V_{\text{trans}}^2 + (V_{\text{mean}} - V_{\text{ref}})^2}$  where  $V_{\text{mean}}$  is in Table 3 and  $V_{\text{ref}}$  is the LSR-velocity of the reference spot (1.6 km s<sup>-1</sup>). Negative and positive represent approaching and receding motions, respectively. <sup>g</sup> Inclination angle of the  $V_{3\text{D}}$  vector with respect to the plane of the sky, obtained from  $i = \tan^{-1}(|V_{\text{mean}} - V_{\text{ref}}|/V_{\text{trans}})$ . <sup>h</sup> All the parameters for Feature 2 are derived from the data taken in the first 3 epochs.

a protostellar jet. The maser velocity gradient parallels a line connecting MAIN and SW masers. It also parallels the NE-SW pair of the Intermediate High Velocity (IHV) CO outflow lobes (PA  $\simeq -150^\circ$ ; BFT95), although on a smaller scale than the 10'' (corresponding to 0.034 pc) scale of the CO lobes. Secondly, the velocity sense of the two flow signatures agrees: the blueshifted masers lie to the NE side and the redshifted masers lie to the SW, the same as found in the velocity structure of the IHV CO outflow lobe pair. Third, the relative proper motion between the MAIN and SW shows expansion, and its direction (PA =  $-131^\circ$ ; Table 4) is almost parallel to the flow line. These results strongly suggest that the maser jet channels along the direction of the line connecting MAIN and SW. It would be difficult to reconcile these motions with interaction of a flow with a protostellar disk.

We assume that the exciting source of the jet is located very near the position of the reference 1.6 km s<sup>-1</sup> spot for the following reasons. First, Feature 5, which hosts the 1.6 km s<sup>-1</sup> spot, shows a single-peaked spectrum over all 4 epochs (Fig. 4), and it did not show a velocity drift (Table 3). Second, the intensity weighted mean position of Feature 5 and position of the 1.6 km s<sup>-1</sup> spot showed a positional coincidence within 0.11 mas over the 4 epochs (see Fig. 6), which is consistent with the result that the reference spot would have a  $FWHM \sim 0.06$  mas derived from the fringe amplitude analysis (Sect. 4.5). Last, the intensity weighted mean positions lie near to a line connecting the MAIN and SW masers, suggesting that the 1.6 km s<sup>-1</sup> spot is located at the expansion center.

Now we try to shed light on the nature of the masers using a simple jet model. We assume that the H<sub>2</sub>O maser emission is excited in the material at the interface between the protostellar jet and the ambient gas, namely, at the surface of the cone whose opening angle is  $2\theta$ . Such a model has successfully explained the distribution of H<sub>2</sub>O masers in the high-mass (proto)star IRAS 20126+4104 (Moscadelli et al. 2000). Figure 8 schematically shows the model: the assumed protostar lies at the apex of the cone. The axis of the cone is inclined

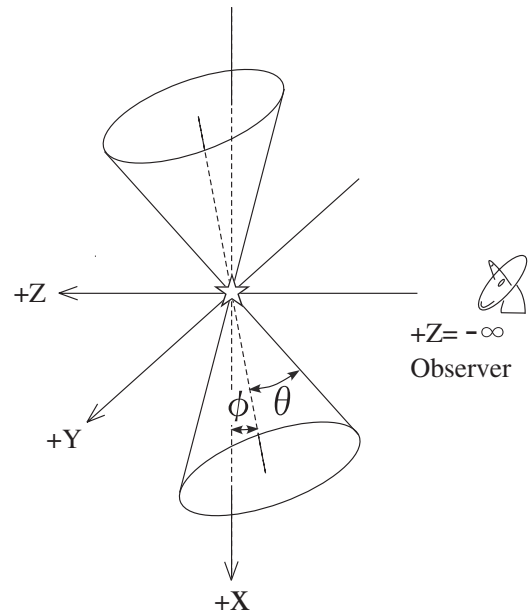


**Fig. 8.** Sketch of the biconical jet model. The  $z$  and  $x$  axes correspond to the line of sight and the jet axis projected on the plane of the sky, respectively. An observer lies at  $z = -\infty$ , and the  $x$ - $y$  plane corresponds to the plane of the sky.

by an angle of  $\phi$  with respect to the plane of the sky. We define a coordinate system whose  $z$  and  $x$  axes are, respectively, parallel to the line of sight and the projection of the jet axis on the sky. To calculate the jet velocities seen by an observer ( $v_z$ ) at  $z = -\infty$ , we consider that the gas moves along straight lines passing through the apex in two opposite directions. Given a power-law velocity profile of  $v(r) = v_0(\frac{r}{R})^\alpha$ , the jet velocity along the line of sight can be written as

$$v_z(x) = v_0 \left\{ \frac{x}{R \cos(\phi + \theta)} \right\}^\alpha \sin(\phi + \theta). \quad (1)$$

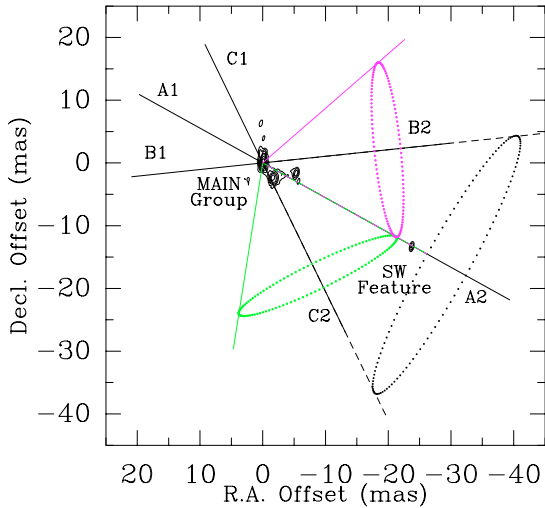


**Fig. 9.** Guide map showing the 3 jet axes that have been taken as cutting lines in the position-velocity diagrams (see text; Fig. 10). To avoid confusion, we present only an outline of each single lobe of the jet. The position angles of the 3 jet axes in the upper panel are  $61^\circ$  for the axis with the labels of A1 and A2,  $101^\circ$  for B1 and B2, and  $28^\circ$  for C1 and C2.

Here we adopt  $v_0$  of  $14.4 \text{ km s}^{-1}$  from the 3D-velocity of the SW maser (Table 4) and its distance of 21 AU from the  $1.6 \text{ km s}^{-1}$  spot for  $R$ . We believe that this assumption is reasonable when we consider other results from VLBA proper motions studies in low- and intermediate-mass YSOs (IRAS 05413–0104:  $64 \pm 22 \text{ km s}^{-1}$  at a distance of 40 AU from the expansion center (Claussen et al. 1998), S106 FIR:  $25\text{--}40 \text{ km s}^{-1}$  at 25 AU (Furuya et al. 2000), IRAS 21391+5802:  $\leq 42 \text{ km s}^{-1}$  at  $\sim 20$  AU (Patel et al. 2000), NGC 2071 IRS3:  $22\text{--}42 \text{ km s}^{-1}$  at 260 AU (Seth et al. 2002)). We thus have the following four free parameters: PA of the projected jet axis to the plane of the sky (i.e., PA of  $x$ -axis),  $\phi$ ,  $\theta$  and  $\alpha$ . By definition, we can give constraints of  $0 < \theta < \pi/2$  and  $0 < |\phi| < \pi/2$ . To apply such a model, we selected 3 possible axes of PA =  $61^\circ$ ,  $101^\circ$  and  $28^\circ$  which we refer to as, respectively, A1–A2, B1–B2 and C1–C2 (see Fig. 9). Note that  $61^\circ$  is the PA of the line connecting the reference spot and the SW maser, and that B1–B2 and C1–C2 are parallel to the two pairs of CO outflow lobes (see Fig. 3 of BFT95). As for the power-law indices of the jet velocity, we considered representative values of  $\alpha = 0$ ,  $+1$  and  $-1$  which characterize constant velocity, accelerating and decelerating jets, respectively.

We compared the observed and calculated velocities in position-velocity (PV) diagrams: the black dots in Fig. 10 represent the PV distribution of the masers along the A1–A2 axis. Here we took the LSR-velocity of  $-1.6 \text{ km s}^{-1}$  as the mean velocity. Figure 10 clearly tells us that the systemic velocity of  $V_{\text{LSR}} = 6 \text{ km s}^{-1}$  (see the inserted panel in Fig. 2) which was derived from the 0.01 pc scale molecular cloud (BFT95) is not valid for the 10 AU scale maser emitting region. We started searching for the best-fit parameters from  $\alpha$ . We found that only an accelerating jet can explain the observed velocity structure whereas both constant velocity and decelerating jets cannot. We thus take  $\alpha = +1$ , leaving us with

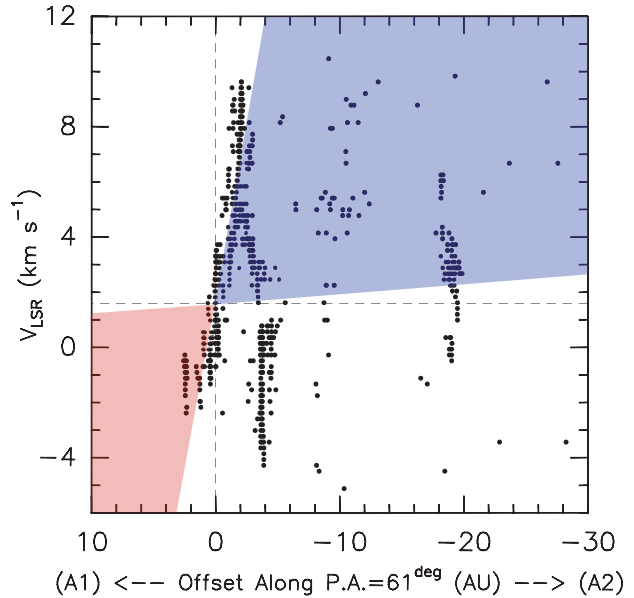


**Fig. 10.** Comparison of the radial velocities from the biconical jet model with the observed LSR-velocities in the position-velocity (PV) diagram along the A1–A2 axis. Here we plotted all of the maser spots detected in the 4 epoch observations. The vertical and horizontal dashed lines, respectively, represent the positions of the reference  $1.6 \text{ km s}^{-1}$  spot. Expected blue- and redshifted radial velocity regions from the model are hatched with blue and red, respectively (see text).

two free parameters –  $\phi$  and  $\theta$ . We obtained the best-fit parameters of  $\phi = -39^\circ$ , and  $\theta = 36^\circ$ . The blue- and red hatched regions in the 1st and 3rd quadrants of Fig. 10, respectively, show the expected LSR-velocity ranges for the blue- and redshifted components. Although the observed maser emission is not excited all over the expected regions, a large opening angle such as  $2\theta \gtrsim 70^\circ$  is required to explain the velocity structure in the 1st and 3rd quadrants. This geometry suggests that the line of sight would match the cone surface (that is,  $|\theta| + |\phi| \sim \frac{\pi}{2}$ ). However, the remaining maser spots in the 4th quadrant, which are Features 13 and 14 (see Fig. 3), are not consistent with the jet model predictions.

Since only the accelerating jet explains the velocity structure, we extended our analysis to the remaining two axes of B1–B2 and C1–C2, keeping  $\alpha = +1$ . The best-fit parameters for the B1–B2, and C1–C2 cases are essentially the same as those obtained from the A1–A2 in the following three senses:

- (i) Requiring a large opening angle ( $2\theta = 72^\circ$  for B1–B2 and  $74^\circ$  for C1–C2), in other words, the PA would have an uncertainty of  $35^\circ$ .
- (ii) The cone is most likely to have a geometry such that the surface where masers are excited is nearly parallel to the line of sight ( $|\theta| + |\phi| = 78^\circ$  for B1–B2, and  $80^\circ$  for C1–C2), namely, the SW masers lie at the either of the two edges of the cone.
- (iii) The LSR-velocities of the spots in Features 13 and 14 cannot be simultaneously reproduced by other spots.

In addition, we performed further analysis by changing the PA through 5° increments, realizing the following points which might jeopardize the above conclusion:

- (a) There is a 4 order of magnitude difference in the spatial scales between our VLBA images and CO (2–1) maps.
- (b) There is no clear association of CO outflows with known driving source(s) (Sect. 4.1; BFT95; Chini et al. 2001).
- (c) The maser emission does not trace the whole of the outflowing gas.

Nonetheless, the analysis with 5° PA steps showed that the above results from (i) to (iii) are valid, and that no range of PA other than from 25° to 110° can be taken.

Of the available observations of this region, our high resolution data has the best opportunity to discern individual sources of outflow. We stress that a single jet model cannot explain the PV structure of Features 13 and 14 which are located at the most western portion of the chain of the MAIN maser features, but show a clear velocity gap with respect to the coherent velocity structure from Features 3 to 12 (see Fig. 3). Can they be used to pinpoint additional sources of outflow, perhaps associated with the other jet-like CO outflows from the region? We examined the velocity structure of the discordant spots in terms of a “multiple jet scenario” by applying the above “single jet model” to “residual PV diagrams”. We subtracted maser spots in the hatched regions in Fig. 10. In addition, we subtracted all the SW spots, assuming that such spots are associated with the “main” jet. Hence, the “residual spots” consist of all the spots in Features 13 and 14, and most of the spots in Features 1–3. “Residual PV diagrams” were made along position angles incremented by 30°, including all the CO outflow position angles. Given the same driving source as the “main” jet, one of the second jet lobes must lie to the NW, which might be characterized by a PA  $\sim 150^\circ$ ,  $2\theta \sim 130^\circ$  and  $\phi \sim 60^\circ$ , but with no symmetrically placed lobe. We are unable to convincingly associate the residual spots with any particular flow geometry or additional discrete source. We speculate that the residual spots are being excited in some shocked regions associated with the “main” jet.

We summarize our jet model analysis by combining the results from i) to iii) with those from the “residual PV” analysis:

1. The majority of the H<sub>2</sub>O masers are most likely to be associated with an accelerating biconical jet whose projected axis has a PA of  $60^\circ \pm 35^\circ$ , and whose opening angle is larger than about 70°.
2. The cone surface enclosing the jet almost matches the line of sight.
3. We could not clearly explain the origin of the remaining maser spots, and speculate that they are being excited in more complex jet-cloud interactions.

We suggest that MMS1 is probably a single star and is the source of the flow exciting the masers lying near it. If there has been no precession(s) of the maser jet and CO outflow(s), our results indicate that the maser jet is most closely associated with the NE–SW pair of the IHV CO lobes because their

axes are almost parallel. The large opening angle of  $\sim 70^\circ$  at a distance of 21 AU from the assumed expansion center is similar to that measured in the intermediate-mass YSO of IRAS 21391+5802 by Patel et al. (2000)—these authors reported an opening angle of  $\sim 110^\circ$  at the 150 AU point from the star. Interestingly these results are also consistent with those from high-mass (proto)stars (Shepherd et al. 2001, and references therein) rather than low-mass protostars where highly collimated CO outflows are generally seen (Richer et al. 2000, and references therein). We suggest that higher luminosity YSOs tend to have poorly collimated jets, and that a similar jet morphology holds for intermediate-mass stars. The conclusion that the masers accelerate agrees with observations of other intermediate-mass YSOs such as S106 FIR (Furuya et al. 1999) and IRAS 21391+5802 (Patel et al. 2000). In addition, this conclusion does not disagree with that from the high-mass star forming region W49N where Gwinn, Moran & Reid (1992) reported that the expansion velocity of the masering gas has a constant velocity of  $\sim 18 \text{ km s}^{-1}$  up to 0.1 pc from the center, beyond which their velocity increases to more than  $200 \text{ km s}^{-1}$ .

Given the complexity of the region seen in the CO maps (BFT95) and the near-IR image (Chen et al. 1997), we believe that sub-arcsecond resolution imaging of the CO outflow and continuum emissions with radio interferometers will associate jets and outflows with their driving sources. These interferometric observations will fill the spatial resolution gap between our AU scale VLBI view of the masers and the 0.01 pc scale single-dish telescope view of the CO outflows. As we have mentioned, IRAS 20050+2720 has displayed H<sub>2</sub>O maser emission at  $V_{\text{LSR}} = -72$  and  $-78 \text{ km s}^{-1}$  since 2003 January, which was not seen during our observations (Sect. 4.2.2). Subsequent monitoring observations using the Green Bank 100-m telescope (Wootten, private communication) showed that these emissions flared to  $\sim 20 \text{ Jy}$  in 2004 October. Together with sub-arcsecond interferometric observations, further VLBA H<sub>2</sub>O maser studies will help to assess the nature of this multiple jet-outflow system, which harbors some of the highest velocity outflowing gas in any star-forming region known to date.

## 6. Summary

We have performed 4-epoch monthly VLBA observations of the H<sub>2</sub>O masers in the intermediate-mass protostar IRAS 20050+2720 MMS1 together with aperture synthesis observations of 3 mm continuum emission with the OVRO array. The main results of this study are summarized as follows.

1. From the VLBA images taken with all 10 antennae, we found the two groups of low-velocity H<sub>2</sub>O maser spots toward the bright millimeter continuum emission peak. One group (the MAIN group) showed intense emission around the cloud velocity, the other (the SW feature) was located at a projected distance of 18.2 AU south-west of the MAIN. The OVRO 3-mm images clearly showed that the bulk of millimeter continuum emission (MMS1) is associated with the low-velocity masers.
2. Using only the south-western antennae of the VLBA, we have succeeded in detecting EHV maser emission

blueshifted by  $99 \text{ km s}^{-1}$  to the cloud velocity. The EHV emission is located at 4400 mas east and 709 mas south of the low-velocity emission. Considering the large 3D separation between the MAIN and EHV features, and the proper motion of the EHV toward the MAIN, we conclude that the EHV emission is not associated with the low-velocity emission. A distinct millimeter continuum source appears to be associated with the EHV masers, which we speculate is the driving source of the EHV emission and which could be an extremely young protostar.

3. The overall structure of the masers in the MAIN group did not change over the 4 epochs. On the other hand, we found that the projected separation between the MAIN group and the SW feature increased by 1.13 mas over the 4 epochs, which corresponds to a transverse velocity of  $14.4 \text{ km s}^{-1}$ . This increment of the separation indicates proper motion(s) of spatially localized masing gas in the MAIN group and/or the SW Features.
4. From the analysis of the velocity field of the masers, we conclude that the majority of the H<sub>2</sub>O masers in IRAS 20050+2720 MMS1 are likely to be associated with an accelerating biconical jet whose opening angle is approximately  $70^\circ$  at a distance of 21 AU from the central star. The presence of such accelerating jet indicates that the central protostar is driving the powerful jet. Moreover, the obtained large opening angle of the jet would support the hypothesis that poor jet collimation is an inherent property of luminous YSOs.

*Acknowledgements.* We are grateful to all of the staff at the VLBA, VLA, and OVRO. R.S.F. thanks C. M. Walmsley for discussion and encouragement. R.S.F. was supported by the postdoctoral fellowship program at INAF, Osservatorio Astrofisico di Arcetri, Italy. Research at the Owens Valley Radio Observatory is supported by the National Science Foundation through NSF grant AST 02-28955.

## References

- André, P., Ward-Thompson, D., & Barsony, M. 1993, *ApJ*, 406, 122
- André, P., Ward-Thompson, D., & Barsony, M. 2000, in *Protostars and Planets IV*, ed. V. Mannings, A. P. Boss, & S. S. Russell (Tucson: University of Arizona Press), 59
- Bachiller, R. 1996, *ARA&A*, 34, 111
- Bachiller, R., Fuente, A., & Tafalla, M. 1995, *ApJ*, 445, L51 (BFT95)
- Brand, J., Cesaroni, R., Caselli, P., et al. 1994, *A&AS*, 103, 541
- Chen, H., Tafalla, M., Greene, T. P., Myers, P. C., & Wilner, D. J. 1997, *ApJ*, 475, 163
- Chini, R., Ward-Thompson, D., Kirk, J. M., et al. 2001, *A&A*, 369, 155
- Claussen, M. J., Wilking, B. A., Benson, P. J., et al. 1996, *ApJS*, 106, 111
- Claussen, M. J., Marvel, K. B., Wootten, A., & Wilking, B. A. 1998, *ApJ*, 507, L79
- Condon, J. J. 1997, *PASP*, 109, 166
- Felli, M., Palagi, F., & Tofani, G. 1992, *A&A*, 255, 293
- Fiebig, D., Duschl, W. J., Menten, K. M., & Tscharnuter, W. M. 1996, *A&A*, 310, 199
- Furuya, R. S., Kitamura, Y., Saito, M., Kawabe, R., & Wootten, H. A. 1999, *ApJ*, 525, 821
- Furuya, R. S., Kitamura, Y., Wootten, H. A., et al. 2000, *ApJ*, 542, L135
- Furuya, R. S., Kitamura, Y., Wootten, H. A., Claussen, M. J., & Kawabe, R. 2001, *ApJ*, 559, L143
- Furuya, R. S., Kitamura, Y., Wootten, H. A., Claussen, M. J., & Kawabe, R. 2003, *ApJS*, 143, 71
- Hofner, P., & Churchwell, E. 1996, *A&AS*, 120, 283
- Gwinn, C. R., Moran, J. M., & Reid, M. J. 1992, *ApJ*, 393, 149
- Molinari, S., Brand, J., Cesaroni, R., & Palla, F. 1996, *A&A*, 308, 573
- Moscadelli, L., Cesaroni, R., & Rioja, M. J. 2000, *A&A*, 360, 663
- Palla, F., Brand, J., Comoretto, G., Felli, M., & Cesaroni, R. 1991, *A&A*, 246, 249
- Palumbo, G. G. C., Scappini, F., Pareschi, G., et al. 1994, *MNRAS*, 266, 123
- Patel, N. A., Greenhill, L. J., Herrnstein, J., et al. 2000, *ApJ*, 538, 268
- Richer, J. S., Shepherd, D. S., Cabrit, S., Bachiller, R., & Churchwell, E. 2000, in *Protostars and Planets IV*, ed. V. Mannings, A. P. Boss, & S. S. Russell (Tucson: University of Arizona Press), 867
- Seth, A. C., Greenhill, L. J., & Holder, B. P. 2002, *ApJ*, 581, 325
- Shepherd, D. S., Claussen, M. J., & Kurtz, S. E. 2001, *Science*, 292, 1513
- Terebey, S., Vogel, S. N., & Myers, P. C. 1992, *ApJ*, 390, 181
- Torrelles, J. M., Gómez, J. F., Rodríguez, L. F., et al. 1998, *ApJ*, 505, 756
- Walker, R. C., Matsakis, D. N., & Garcia-Barreto, J. A. 1982, *ApJ*, 255, 128
- Walker, R. C. 1981, *AJ*, 86, 1323
- Wilking, B. A., Blackwell, J. H., Mundy, L. G., & Howe, J. E. 1989, *ApJ*, 345, 257
- Wilking, B. A., Claussen, M. J., Benson, P. J., et al. 1994, *ApJ*, 431, L119
- Wilner, D. J., & Welch, W. J. 1994, *ApJ*, 427, 898
- Wootten, A. 1989, *ApJ*, 337, 858